PDR diagnostics study with CLOUDY

Rui Xue and Maohai Huang

National Astronomical Observatories, Chinese Academy of Sciences, Beijing 100012, China;
jerryxue@gmail.com

Abstract A series of plane-parallel photodissociation region (PDR) models are calculated using the spectral synthesis code CLOUDY. These models span a wide range of physical conditions, with gas densities of $n = 10^2 - 10^6 \, \mathrm{cm}^{-3}$ and incident far-ultraviolet (FUV) fields of $G_0 = 10^0 - 10^6$ (where G_0 is the FUV flux in units of the local interstellar value), which are comparable with various astrophysical environments from interstellar diffuse clouds to the dense neutral gas around galactic compact H II regions. Based on the calculated results, we study the thermal balance of PDR gas and the emissions of [C II], [C I] and [O I] fine-structure lines under different physical conditions. The intensities and strength ratios of the studied lines, which are frequently used as PDR diagnostics, are presented using contour diagrams as functions of n and G_0. We compare the calculated PDR surface gas temperatures T_s with those from Kaufman et al. and find that T_s from our models are systematically higher over most of the adopted n-G_0 parameter space. The predicated line intensities and ratios from our work and those from Kaufman et al. can be different by a factor greater than 10, and such large differences usually occur near the border of our parameter space. The different methods of treating the dust grain physics, the change of H_2 formation and dissociation rates, and the improvement in the radiation transfer of line emissions in our CLOUDY models are likely to be the major reasons for the divergences. Our models represent an up-to-date treatment of PDR diagnostic calculations and can be used to interpret observational data. Meanwhile, the uncertainties in the treatment of microphysics and chemical processes in PDR models have significant effects on PDR diagnostics.

Key words: infrared: ISM — ISM: clouds — ISM: molecules — methods: numerical

1 INTRODUCTION

Widespread photodissociation regions (PDRs) play an important role in the physical and chemical evolution of the atomic and molecular gas in our galaxy (Hollenbach & Tielens 1999). The study of PDRs not only helps us to understand their various physical and chemical processes, but also provides powerful diagnostic tools to reveal the physical conditions of the interstellar medium (ISM), the characteristics of local star-forming regions, and even the evolutionary histories of distant galaxies.

Many modeling efforts have been made to establish the relationship between the observable emissions of PDRs and their physical and chemical properties (Tielens & Hollenbach 1985; van Dishoeck & Black 1986; Wolfire et al. 1990; Stoerzer et al. 1996; Kaufman et al. 1999). These works have been tested and improved when applied in the interpretations of numerous observations. As abundant infrared/submillimeter spectra and images became available from space/ground-based equipments, such as the *Infrared Space Observatory* (*ISO*), the Caltech Submillimeter Observatory (CSO), and the

Antarctic Submillimeter Telescope and Remote Observatory (AST/RO), in the last twenty years, PDR models have evolved to take account of the more detailed and realistic treatment of physical and chemical processes in PDRs. Since such models usually include a self-consistent treatment of the thermal and chemical balance in PDR gas, coupled with radiation transfer problems, most of them have nowadays become sophisticated and they all strongly depend on numerical methods (see Röllig et al. 2007 for a summary of various PDR codes).

Based on the improved classical PDR model from Tielens & Hollenbach (1985), the infrared diagnostic diagrams produced by Wolfire et al. (1990) and Kaufman et al. (1999) (K99, hereafter), have become a standard tool for observers to evaluate the physical characteristics of PDRs. Derived from numerical results, these diagrams show how the intensities or strength ratios of important PDR diagnostic lines, such as [O I], [C II] and [C I], vary as functions of the strength of incident far-ultraviolet (FUV) field G_0 and the PDR gas density n under certain modeling assumptions. The limited free parameters in their works allow one to compare the model predictions with observational data using the precalculated results efficiently.

Recent development of the spectral synthesis code CLOUDY allows its application for self-consistent calculations of PDR thermal and chemical structures. By taking advantage of its original function for the simulation of ionized gas, Abel et al. (2005) demonstrated CLOUDY's capability to model H II regions and associated PDRs continuously. In addition, they performed a parameter study for several important diagnostic lines emerging from the PDR-H II complex. Röllig et al. (2007) described a detailed technical comparison of various PDR codes, including CLOUDY and the code used by the serial works of Tielens & Hollenbach (1985), Wolfire et al. (1990) and K99 (the THWK code, hereafter), etc. However, it is not well known how much difference exists between the flexible CLOUDY and the widely used THWK PDR code when they are used to analyze the same observational results. Specifically, how differently do the two codes produce infrared diagnostic diagrams for the most frequently used PDR diagnostic lines, [O I], [C II] and [C I], under similar modeling assumptions? How divergent could the physical properties of PDRs be which were derived from the same observational results?

In this work, we calculate a series of PDR models using the spectral synthesis code CLOUDY to study the thermal balance of PDR gas and the emissions of [O I], [C II] and [C I]. We produce infrared diagnostic diagrams of the studied lines and evaluate their behaviors over a wide physical range of PDRs. We make comparisons between our results and those from K99 which are based on the THWK code and examine their differences in the analysis of observed emissions. In Section 2, we describe the details of our PDR model calculations using CLOUDY. In Section 3, we present the calculated PDR surface gas temperatures and the infrared diagnostic diagrams from our modeling results, and include comparisons with the predications from K99. In Section 4, we discuss the differences of the PDR models from our work and from K99, as well as general uncertainties of using model predications to interpret observational data. Conclusions are given in Section 5.

2 PDR MODELS

Our PDR model calculations are performed with version 07.02 of CLOUDY, described by Ferland et al. (1998). Since our study is targeted at reproducing infrared diagnostic diagrams using CLOUDY and making comparisons with the results of K99 using these diagrams, we adopt the identical modeling assumptions and input parameters with K99 as much as possible. Table 1 summarizes the basic parameters and assumptions for our PDR models. We describe the details as follows.

Although CLOUDY includes the feature to simulate pressure-balanced or spherical PDRs (Abel et al. 2005; Pellegrini et al. 2007), we adopt the plane-parallel geometric configuration and the constant-density structure in our PDR models. The incident radiation field is extinguished above 13.6 eV and the wavelength dependence of FUV flux is set equal to the interstellar FUV field (Habing 1968). We use visual extinction A_V to measure the depth of the PDR. The calculations of thermal and chemical balance and radiation transfer start from the PDR face illuminated by FUV photons where $A_V = 0$ mag, and stop when A_V reaches 10 mag.

Table 1 Details of the Calculated PDR Models

Configuration/Parameters	Assumption/Value/Reference
Geometry	Plane-Parallel Slab
Density structure	Constant Density
Depth range A_V (mag)	$0 - 10$
Density range n (cm^{-3})	$10^2 - 10^6$
FUV flux range G_0[a]	$10^0 - 10^6$
Turbulence velocity (km s^{-1})	1.5
Carbon abundance[b]	1.4×10^{-4}
Oxygen abundance[b]	3.0×10^{-4}
Silicon abundance[b]	1.7×10^{-6}
Sulfur abundance[b]	2.8×10^{-5}
Iron abundance[b]	1.7×10^{-7}
Magnesium abundance[b]	1.1×10^{-6}
Chemical reaction rates	UMIST99 dataset (Le Teuff et al. 2000)
H$_2$ formation rate	Cazaux & Tielens (2002)
H$_2$ dissociation rate	Bertoldi & Draine (1996)
Visual extinction to hydrogen column density A_V/N (mag cm^2)	5×10^{-22}
PAH abundance $n_C(\text{PAH})/n$	3×10^{-6}

[a] The incident FUV field of PDR is usually characterized using G_0, which is the absolute strength of FUV flux between 6 and 13.6 eV relative to the value of the background interstellar radiation field, 1.6×10^{-3} erg cm^{-2} s^{-1} (Habing 1968).
[b] Gas phase abundances relative to that of the hydrogen nucleus.

Two of the most important physical parameters of PDR models, determining their thermal and chemical structures when the intrinsic properties of dust grains and gas are given, are the strengths of incident FUV fields G_0 and the PDR gas density n (Tielens & Hollenbach 1985). The former is usually expressed by the absolute FUV flux relative to the value of the background interstellar radiation field (1.6×10^{-3} erg cm^{-2} s^{-1}, Habing 1968), and the latter is the volume density of the hydrogen nucleus in PDR gas. In our model study, G_0 and n are the only variable parameters, which are increased from 10^0 to 10^6 and 10^2 to 10^6 cm^{-3} by 0.25 dex, respectively. Therefore, a total of 425 calculations are performed to build a grid of PDR models. The adopted parameter ranges of G_0 and n cover various astrophysical environments, from interstellar diffuse clouds to the dense neutral gas around galactic compact H II regions.

Our models include a Gaussian turbulence velocity field of 1.5 km s^{-1}, which is the same as that adopted in K99. The gas-phase abundances of important elements are listed in Table 1, taken from Savage & Sembach (1996) for cool diffuse clouds and identical to those adopted in K99. The chemical reaction rates in our models are from the updated UMIST99 dataset (Le Teuff et al. 2000). The H$_2$ formation rate on dust grains is derived from Cazaux & Tielens (2002), which is dependent on grain temperature. The H$_2$ dissociation rate is derived from Bertoldi & Draine (1996). The adopted formation and dissociation rates of H$_2$ are different from those in K99. They use the observed formation rate per unit volume of 3×10^{-17} cm^3 s^{-1} (Jura 1974) and the dissociation rate for an unshielded H$_2$ molecule of 4.7×10^{-11} s^{-1} (Abgrall et al. 1992).

We adopt the built-in ISM dust grain model of CLOUDY using the command 'grains ISM'. This dust model includes both graphite and silicate grains with sizes ranging from 5×10^{-3} μm to 0.25 μm. The size distribution is appropriate for the ISM in our galaxy, and the model can reproduce the extinction property of $R_V = 3.1$. The details of the grain physics in CLOUDY are described by van Hoof et al. (2004), and grain charging, heating, temperature and drift velocity are self-consistently determined for grains of every size. The dust abundance in our models is adjusted to achieve the ratio of visual extinction to hydrogen nucleus column density $A_V/N = 5 \times 10^{-22}$ mag cm^2. Our models include size-resolved polycyclic aromatic hydrocarbons (PAHs) with the same size distribution used by Bakes & Tielens (1994). The adopted abundance of carbon atoms in PAHs, $n_c(\text{PAH})/n_H$, is 3×10^{-6}. The calculations of PAH charging and heating follow the description given by Bakes & Tielens (1994). The

treatment of the cosmic ray ionization and grain charge transfer processes in CLOUDY is explained in Abel et al. (2005). In our calculations, gas depletion on grains is not considered although CLOUDY can model this process.

3 MODEL RESULTS AND COMPARISONS

In this section, we present the calculated results of the PDR surface gas temperature T_s, and the emissions of [O I], [C II] and [C I] as functions of n and G_0, along with the corresponding results from K99, so that we can compare the model predications of CLOUDY and the THWK code under similar physical and chemical conditions.

3.1 Surface Gas Temperature

Here, we present calculated gas temperatures at the PDR surface T_s, which can help us to evaluate the thermal balance of PDR gas in the low-extinction region that dominates [O I] and [C II] emissions. Figure 1 shows calculated T_s as functions of G_0 and n. For a given n, T_s generally rises with G_0 because the FUV flux is the heating source of PDR gas. The dependence of T_s on n is more complicated. When n is lower than the critical densities of the major cooling transitions [O I] 63 μm and [C II] 158 μm ($\sim 10^4 - 10^5$ cm^{-3}), T_s generally decreases with increasing n, because the gas cooling rate per volume increases faster than the heating rate before the [C II] and [O I] reach thermalization (Kaufman et al. 1999). In the region with higher density, heating from the collisional deexcitation of FUV pumped H$_2$ becomes important (Hollenbach & Tielens 1999), and the additional heating makes T_s rise rapidly with the increase of n.

The model results of K99, including the PDR surface gas temperatures, line intensities and ratios of [O I], [C II] and [C I] diagnostic lines, are available in FITS format from the Photodissociation Region Toolbox[1]. We reproduce their T_s contour diagram based on these data, and show it in the left panel of Figure 2. The right panel of Figure 2 is the ratio of T_s from our work and from K99. Over most of our n-G_0 parameter space, the ratio is greater than 1, indicating that T_s from our work is generally higher. The largest difference occurs in the lower-right corner with $n > 10^5$ cm^{-3} and $G_0 < 10^2$, where our calculated T_s can be more than a factor of 10 larger than that from K99.

3.2 PDR Line Diagnostics

The [O I], [C II] and [C I] fine-structure lines are the most frequently used PDR diagnostics due to their rich abundances, relatively easy excitation conditions, and important roles in the thermal and chemical balance of PDR gas. Table 2 summarizes their prominent transitions at the wavelengths of mid-infrared and submillimeter.

Table 2 [O I], [C II] and [C I] Diagnostics

Species	λ (μm)	Transition	ΔE (K)	n_{cr}[a] (cm^{-3})
O^0	63.2	$^3P_1 \rightarrow {}^2P_2$	228	4.7×10^5
O^0	145.6	$^3P_0 \rightarrow {}^3P_1$	98	9.5×10^4
C$^+$	157.7	$^2P_{3/2} \rightarrow {}^2P_{1/2}$	92	2.8×10^3
C^0	370	$^3P_2 \rightarrow {}^3P_1$	39	2.8×10^3
C^0	610	$^3P_1 \rightarrow {}^3P_0$	24	4.7×10^2

[a]These values are taken from Tielens & Hollenbach (1985).

The emissions of [O I], [C II] and [C I] fine-structure lines are sensitive to the physical and chemical conditions of PDR. The contour diagrams from K99 show how the important diagnostic line intensities and ratios vary with changes in G_0 and n, and have become very useful for observers to evaluate
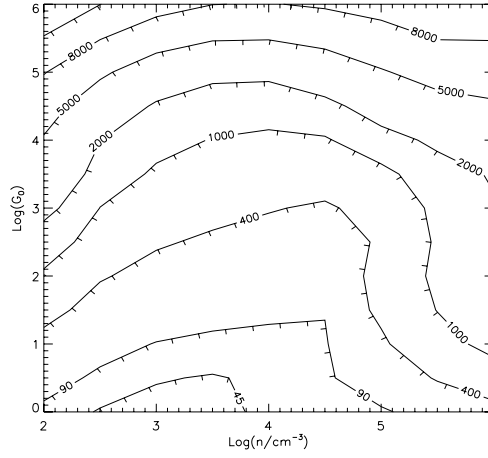
[1] *http://dustem.astro.umd.edu/pdrt*

Fig. 1 Contour diagram of the gas temperature at the PDR surface (T_s) from our calculations, in units of K.
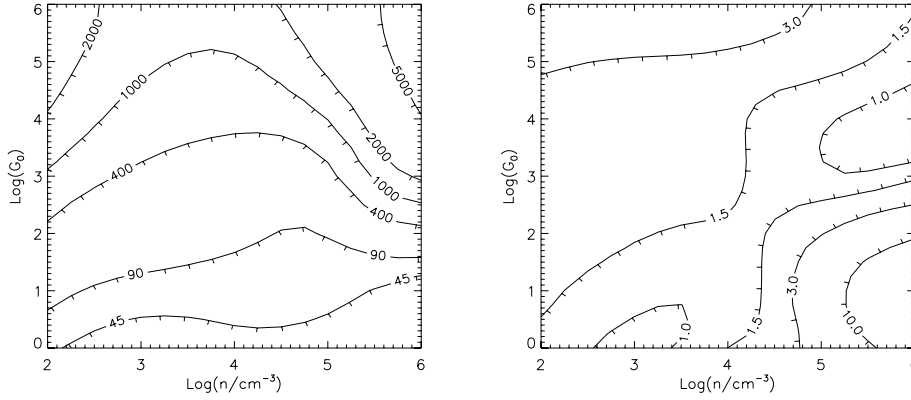

Fig. 2 *Left panel*: Contour diagram of T_s from K99, in units of K. *Right panel*: Contour diagram for the ratio of T_s from our work and from K99. Our calculated T_s values are systematically higher over most of our parameter space. The largest difference of one order of magnitude occurs in the lower-right corner where $n \gtrsim 10^5 \, \mathrm{cm}^{-3}$ and $G_0 \lesssim 10^2$.

the physical characteristics of PDRs (e.g. Minamidani et al. 2008; Okada et al. 2003; Contursi et al. 2002; Hunter et al. 2001). In the following section, we present similar contour diagrams based on our model calculations using CLOUDY. We also include detailed comparisons with the corresponding results of K99 over the adopted n-G_0 parameter space.

3.2.1 [C II] 158 μm

Figure 3 shows the contour diagram of the [C II] 158 μm intensity, I_{158}, from our calculations within the given parameter space. In our work, the intensities of all fine-structure lines are their integrated line fluxes divided by 2π, in units of $\mathrm{erg\,cm}^{-2}\,\mathrm{s}^{-1}\,\mathrm{sr}^{-1}$. For a given n, I_{158} is more sensitive to G_0 in the region with $G_0 \lesssim 10^{2.5}$, where the gas temperature is lower than its excitation temperature of 92 K. In the
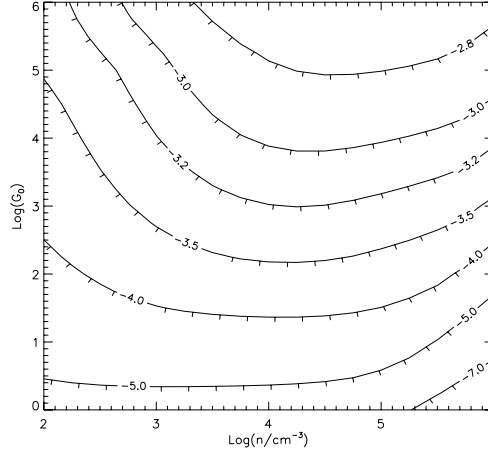
Fig. 3 Contour diagram of the intensity of [C II] 158 μm (I_{158}) from our calculations, in units of erg cm^{-2} s^{-1} sr^{-1}. The values are in the logarithmic scale.
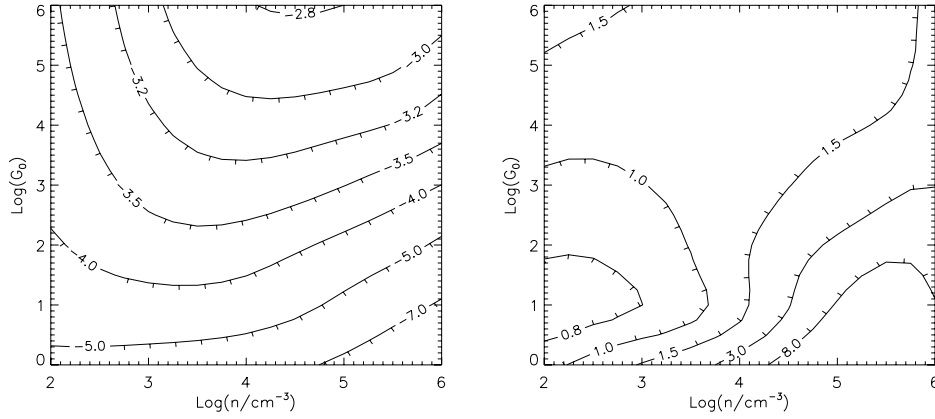

Fig. 4 *Left panel*: Contour diagram of I_{158} from K99 in units of erg cm^{-2} s^{-1} sr^{-1}. The values are in the logarithmic scale. *Right panel*: Contour diagram for the ratio of I_{158} from our work and from K99. The difference can be greater than a factor of 8 when $G_0/n < 10^{-3}$ cm^3.

region with higher G_0, I_{158} still rises with G_0 mainly due to the slow increase of the column density of C$^+$, N_{C^+}. The density dependence of I_{158} is a little more complicated. When n is lower than the critical density of [C II] 158 μm ($\sim 3 \times 10^3$ cm^{-3}), I_{158} increases rapidly with n since [C II] doesn't reach thermalization. In the high-density region where $n > 10^5$ cm^{-3}, I_{158} drops rapidly because the increasing gas density enhances gas shielding of the FUV flux ionizing the atomic carbon and reduces N_{C^+}.

The left panel of Figure 4 shows I_{158} from K99. We find that the contour diagrams of I_{158} from different approaches show similar tendencies in the n and G_0 dependence. However, in our calculations, the drop of N_{C^+} with increasing n starts to affect the intensity of [C II] at a higher density ($> 10^{4.5}$ cm^{-3}). The right panel of Figure 4 shows the ratio of I_{158} from our work and from K99, indicating that our calculated I_{158} is systematically larger except in the region where $n \lesssim 10^{3.5}$ cm^{-3} and $G_0 \lesssim 10^{3.5}$. The difference of I_{158} from our work and from K99 can be greater than a factor of 8 when $G_0/n < 10^{-3}$ cm^3.
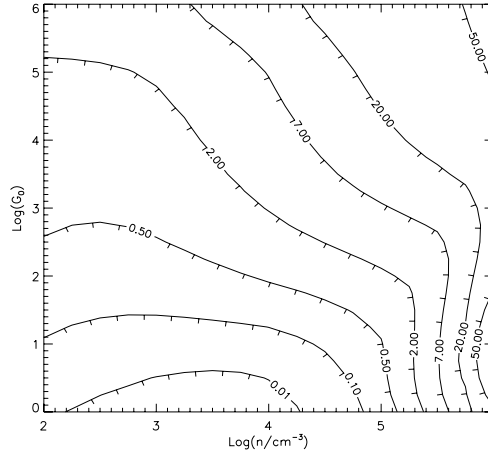
Fig. 5 Contour diagram of the strength ratio of [O I] 63 μm and [C II] 158 μm (I_{63}/I_{158}) from our calculations. To the right of a straight line connecting (4.5, 0) and (6, 3) in the $\log(n) - \log(G_0)$ coordinates, I_{63}/I_{158} becomes strongly dependent on n and insensitive to G_0.
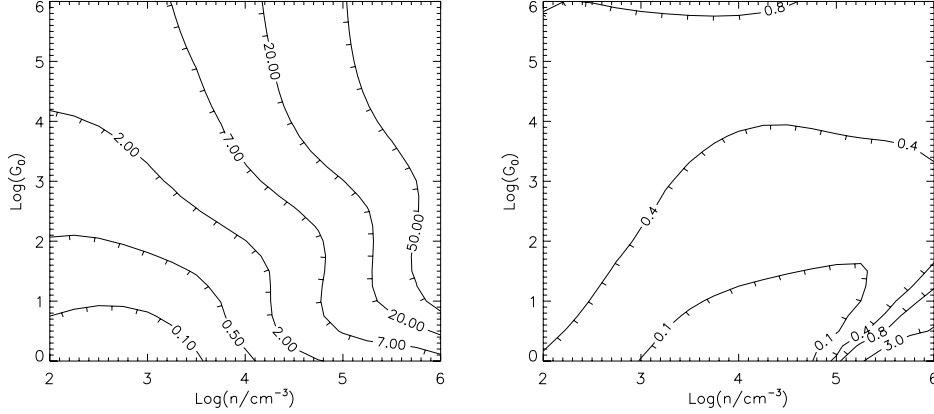

Fig. 6 *Left panel*: Contour diagram of I_{63}/I_{158} from K99. *Right panel*: Contour diagram for the ratio of I_{63}/I_{158} from our work and from K99. Our calculated I_{63}/I_{158} values are generally less than those from K99 over most of the parameter space.

3.2.2 [O I] 63 μm / [C II] 158 μm

Figure 5 shows the calculated strength ratio of [O I] 63 μm and [C II] 158 μm, I_{63}/I_{158}, as functions of G_0 and n. I_{63}/I_{158} is sensitive to both n and G_0 when G_0 is larger than 10^3. To the right of a straight line connecting (4.5, 0) and (6, 3) in the $\log(n) - \log(G_0)$ coordinates, I_{63}/I_{158} becomes strongly dependent on the density and insensitive to G_0.

The left panel of Figure 6 shows I_{63}/I_{158} from K99. Comparing Figure 6 with Figure 5, we find that the I_{63}/I_{158} contour diagrams from the two approaches have significantly different behaviors when $G_0/n < 10^{-4}$ cm^3. The result from K99 shows that I_{63}/I_{158} is mainly dependent on G_0, which disagrees with our predication of the strong density dependence and very weak G_0 dependence. The right
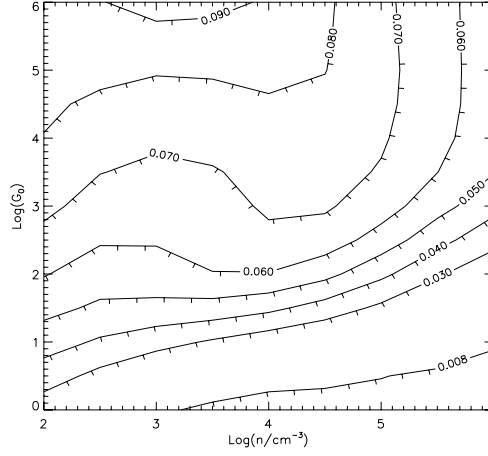
Fig. 7 Contour diagram of the strength ratio of [O I] 145 and 63 μm (I_{145}/I_{63}) from our calculations. In the region with $G_0 > 10^3$ and $n < 10^5$ cm^3, I_{145}/I_{63} shows weak n and G_0 dependence and only varies by a factor of less than 2.
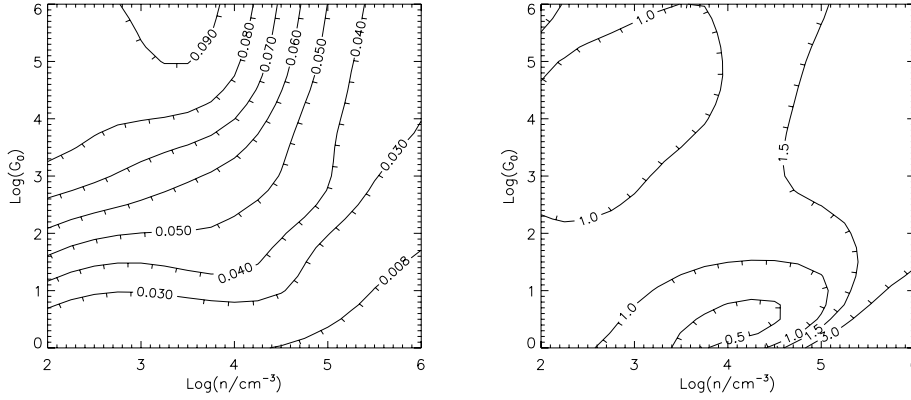

Fig. 8 *Left panel*: Contour diagram of I_{145}/I_{63} from K99. *Right panel*: Contour diagram for the ratio of I_{145}/I_{63} from our work and from K99. This ratio diagram indicates that the estimations of I_{145}/I_{63} from the two approaches agree better than 50% in the parameter space with $n < 10^{4.5}$ cm^{-3} and $G_0 > 10$.

panel of Figure 6 shows the ratio of I_{63}/I_{158} from our work and from K99. The ratio diagram indicates that I_{63}/I_{158} values from our calculations are generally less than those from K99 over most of the parameter space. The only exception occurs in a small area of the lower-right corner, where our I_{63}/I_{158} becomes significantly higher. The difference of I_{63}/I_{158} is partly caused by the underestimation of I_{158} in K99 (see the right panel of Fig. 4).

3.2.3 [O I] 145 μm / [O I] 63 μm

Figure 7 shows our calculated strength ratio of [O I] 145 μm and 63 μm, I_{145}/I_{63}, as functions of G_0 and n. I_{145}/I_{63} is strongly sensitive to G_0 when the gas temperature is not much higher than the

excitation temperatures of the two transitions ($T \lesssim 200 - 300$ K or $G_0 \lesssim 10^2$). When $G_0 > 10^3$, I_{145}/I_{63} is weakly dependent on G_0 and sensitive to n between the critical densities of the two transitions ($1 \times 10^5 \sim 5 \times 10^5$ cm^{-3}). In the region with $G_0 > 10^3$ and $n < 10^5$ cm^3, I_{145}/I_{63} shows weak n and G_0 dependence and only varies by a factor of less than 2.

The left panel of Figure 8 shows I_{145}/I_{63} from K99. The major difference between Figures 7 and 8 is that I_{145}/I_{63} from K99 decreases faster with increasing n in the high-density region ($n > 10^4$ cm^{-3}). The right panel of Figure 8 shows the ratio of I_{145}/I_{63} from our work and from K99. This ratio diagram indicates that the estimations from these two approaches agree better than 50% in the parameter space with $n < 10^{4.5}$ cm^{-3} and $G_0 > 10$. Our estimated I_{145}/I_{63} is significantly larger than that of K99 when $n > 10^5$ cm^{-3}. The difference can be larger than a factor of 3 when $G_0/n < 10^{-4.5}$ cm^3.

3.2.4 [C I] 609 μm

The [C I] fine-structure line emerges from the region with higher extinction than [C II] or [O I]. It is easily excited due to low excitation temperatures (only 24 K and 39 K for [C I] 610 μm and 370 μm, respectively) and small critical densities. Figure 9 shows our calculated intensity of [C I] 609 μm, I_{609}, as functions of G_0 and n. We find that the entire dynamical range of I_{609} is ~ 30 over our parameter space. For a given n, I_{609} increases with G_0. For a given G_0, I_{609} generally rises with increasing n when the density is below 10^5 cm^{-3}. In the parameter space with higher density, I_{609} drops rapidly with n because the photodissociation of carbon-containing molecules becomes weaker and reduces the C^0 column density, N_{C^0}.

The left panel of Figure 10 shows I_{609} from K99. The major difference between Figure 9 and Figure 10 is that in the models of K99, the decreasing of N_{C^0} starts to affect I_{609} significantly at a lower density ($\sim 10^{3.5}$ cm^{-3}). The right panel of Figure 10 shows the ratio of I_{609} from our calculations and from K99. This indicates that I_{609} from different approaches agrees better than 50% over the parameter space with $n < 10^{4.5}$ cm^{-3}. The largest divergence occurs in the upper-right corner of our parameter space, which can be greater than a factor of 4.

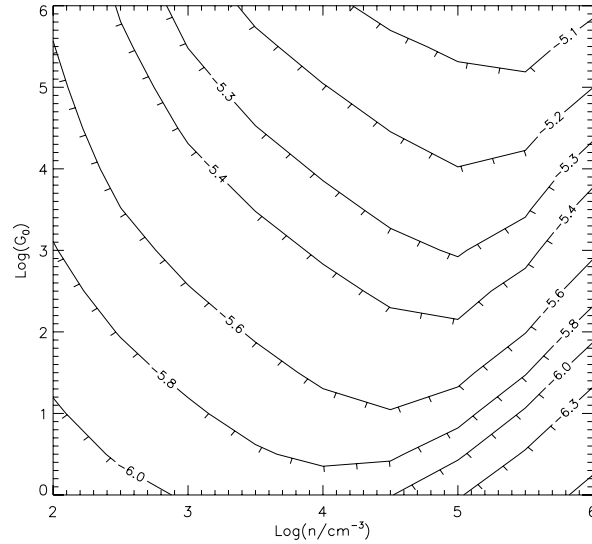**Fig. 9** Contour diagram of the calculated intensity of [C I] 609 μm (I_{609}) in units of erg cm^{-2} s^{-1} sr^{-1}. The values are in the logarithmic scale. The entire dynamic range of the intensity is ~ 30.
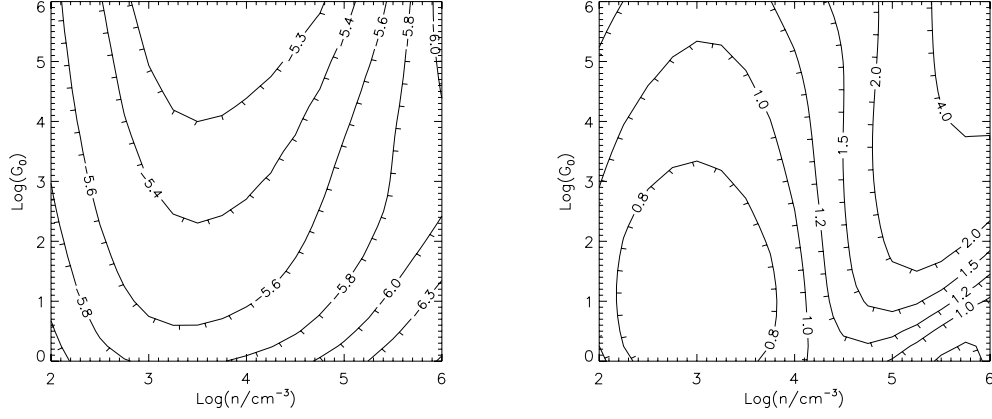
Fig. 10 *Left panel*: Contour diagram of I_{609} from K99, in units of $\mathrm{erg\,cm^{-2}\,s^{-1}\,sr^{-1}}$. The values are in the logarithmic scale. *Right panel*: Contour diagram for the ratio of I_{609} from our work and from K99. I_{609} from different approaches agrees better than 50% when $n < 10^{4.5}\,\mathrm{cm^{-3}}$.

3.2.5 [C I] 370 μm / [C I] 609 μm

Figure 11 shows the strength ratio of [C I] 370 μm and 609 μm, I_{370}/I_{609}, from our calculations. I_{370}/I_{609} only varies by a factor of ~ 20 over the entire parameter space. In general, I_{370}/I_{609} shows weak density dependence after the two transitions reach thermalization ($n \gtrsim 10^4\,\mathrm{cm^{-3}}$).

The left panel of Figure 12 shows I_{370}/I_{609} from K99. The right panel is the ratio of I_{370}/I_{609} from our work and from K99. The ratio diagram indicates that I_{370}/I_{609} from different approaches agrees better than a factor of 2, except that in the lower-left corner of our parameter space where $n \lesssim 10^{3.5}\,\mathrm{cm^{-3}}$ and $G_0 \lesssim 10^{2.5}$.
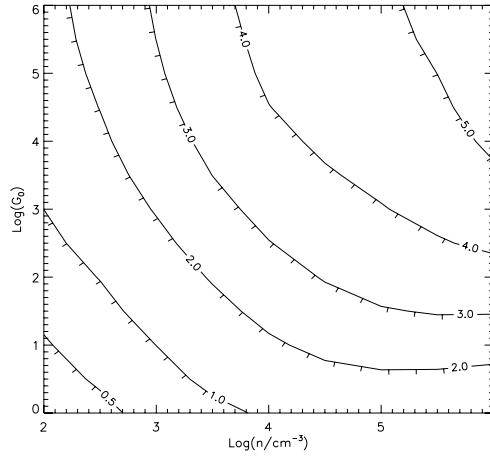

Fig. 11 Contour diagram of the strength ratio of [C I] 370 and 609 μm (I_{370}/I_{609}) from our calculations.
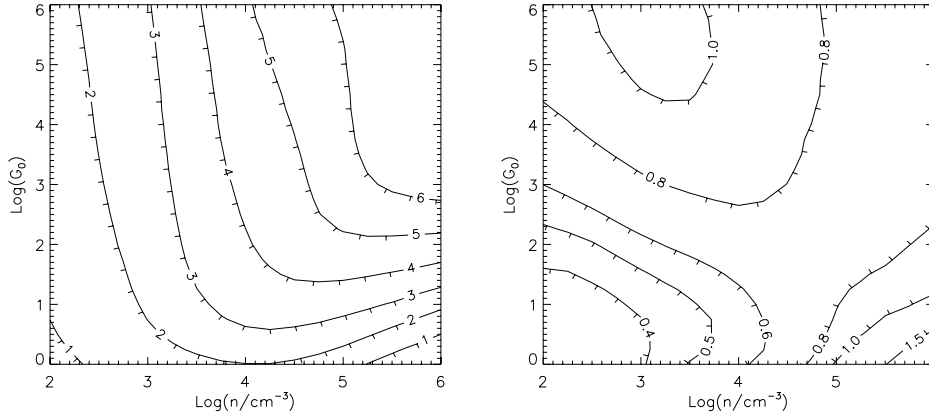
Fig. 12 *Left panel*: Contour diagram of I_{370}/I_{609} from K99. *Right panel*: Contour diagram for I_{370}/I_{609} from our work and from K99. I_{370}/I_{609} from different approaches agrees better than a factor of 2 except that in the lower-left corner of our parameter space where $n \lesssim 10^{3.5}\,\mathrm{cm}^{-3}$ and $G_0 \lesssim 10^{2.5}$.

4 DISCUSSION

Our contour diagrams of line intensities and strength ratios can be used as a diagnostic tool to evaluate n and G_0 of PDRs given the assumptions and input parameters in our models. However, significant differences exist between the model predications of PDR surface temperatures and the emissions of [O I], [C II] and [C I] from our work and those from K99. In this section, we discuss the major differences between our PDR models and those of K99 beyond the behaviors of numerical results, plausible reasons for the divergence in the modeling results, and general uncertainties of using PDR model predications to interpret observations.

4.1 Differences in Modeling Details

Although our CLOUDY models are optimized for a comparison with those of K99, there are still differences between the PDR models from our work and from K99 in the treatment of several important PDR physical and chemical processes.

One of the major differences is in the grain physics, which determines the grain photoelectric (PE) heating and therefore the thermal balance of PDR gas. In our CLOUDY model, the dust grains and PAHs are size-resolved with a distribution appropriate for the ISM of our galaxy. The PE heating and charging are determined for graphite, silicate and PAH components of every size, respectively. However, in the THWK PDR code used by K99, the grain model follows the semi-analytical description of Tielens & Hollenbach (1985) and is not size-resolved. van Hoof et al. (2001) show that calculations using size-resolved grain models of CLOUDY yield more accurate results for the PE heating and collisional cooling rates of the gas by the grains. Therefore, our treatment of grain physics is more physically realistic.

Another major difference between our PDR models and those of K99 is the formation and dissociation rates of H_2. We adopt the temperature dependent H_2 formation rate from Cazaux & Tielens (2002), different from the constant rate of $3 \times 10^{-17}\,\mathrm{cm}^3\,\mathrm{s}^{-1}$ in K99. Our H_2 dissociation rate is from Bertoldi & Draine (1996), which considers the self-shielding effect using the approximation given by Draine & Bertoldi (1996). This rate is different from the constant value of $4.7 \times 10^{-11}\,\mathrm{s}^{-1}$ in K99, but agrees well with the predication from the detailed time-consuming H_2 molecular model built in CLOUDY (Abel et al. 2004). The change of formation and dissociation rates of H_2 may significantly affect the position of the H^0/H_2 transition zone and therefore the H_2 abundance gradient in the low-extinction region of PDRs. As a consequence, this change also affects the heating from the collisional deexcitation of H_2,

and gives significant uncertainties of PDR thermal and chemical balance if this process is dominant in gas heating.

Finally, the treatment of radiation transfer of line emissions is somewhat different in CLOUDY and the THWK code. In our CLOUDY models, we use iteration calculations to achieve better radiation transfer solutions for both cooling lines and the other observational lines. In the K99 models, the analytical equation for the escape probability from de Jong et al. (1980) was adopted to evaluate the emissions of cooling lines. This may underestimate the cooling rates if the cooling emissions are optically thin (Tielens & Hollenbach 1985).

4.2 Divergences in Model Predications

The grain PE effect dominates the gas heating at the PDR surface over most of our parameter space. The heating from the collisional deexcitation of H_2 also becomes important when $G_0/n \lesssim 4 \times 10^{-2}\,\mathrm{cm}^3$ (Hollenbach & Tielens 1999). Since there is no significant difference between CLOUDY and the THWK code in the treatment of major gas cooling mechanisms at the PDR surface, the generally higher T_s from our CLOUDY models should result from the divergence in gas heating, caused by different grain physics models and treatment of H_2 formation and dissociation. For a model with given n and G_0, the differences mentioned above not only affect T_s, but also change the thermal balance and chemical structure over the entire PDR model. Therefore, considering the different approaches for radiation transfer problems, it is not surprising that the emergent line intensities and ratios produced by CLOUDY and the THWK code are different. In Section 3.2, we showed that the line intensities and ratios of [O I], [C II] and [C I] fine-structure lines can be different by a factor greater than 10 in some areas of our parameter space. However, the largest divergence usually occurs in the border of our parameter space. The agreement of the presented line intensities and ratios of [O I] and [C I] is better than 50% when $G_0 > 10^{2.5}$ and $n < 10^{4.5}\,\mathrm{cm}^{-3}$.

4.3 Applicability and Uncertainties in Interpreting Observations

Our calculated PDR models are based on the up-to-date values of chemical reaction coefficients, atomic and molecular data, and H_2 formation/destruction rates, as well as the state-of-the-art methods of treating the PE heating and radiation transfer of line emissions in PDR gas. Therefore, our results represent the most current improved PDR diagnostics diagrams, which are applicable to observational data.

Meanwhile, from the standpoint of observers, the large divergences between our results and those of K99 indicate that, in general, caution must be used when applying the diagnostic contour diagrams of PDR models to analyze observed emissions. In the PDR code comparison study of Röllig et al. (2007), they have found significant scattering among different PDR codes in their thermal balance and line emission predications, even under a simple astrophysical condition. Meijerink et al. (2007) built a similar grid of PDR models using their own PDR code and found that the calculated surface gas temperatures were higher than those from K99. Röllig et al. (2006) presented the change in PDR heating/cooling and [C II] intensities as a function of metallicity Z. All of these works suggest that there are large uncertainties in predications of PDR emissions among different PDR codes and modeling assumptions. For example, K99 estimated that the average PDR density and G_0 for M82 are $10^4\,\mathrm{cm}^{-3}$ and $10^{3.5}$, respectively, by comparing the observed $I_{63}/I_{158} = 8.24$ and $I_{145}/I_{63} = 0.064$ with their corresponding strength ratio contour diagrams. However, using the I_{63}/I_{158} and I_{145}/I_{63} contour diagrams from our grid of PDR models, we found a density of $\sim 10^{5.2}\,\mathrm{cm}^{-3}$ and G_0 of $\sim 10^{3.1}$. If we compare the observed $I_{63}/I_{158} = 8.24$ and $I_{370}/I_{609} = 4.3$ (Stutzki et al. 1997) of M82 with the diagnostic contour diagrams produced by Meijerink et al. (2007), the derived n and G_0 can be $10^{4.8}\,\mathrm{cm}^{-3}$ and $10^{3.3}$. The above example shows that our up-to-date models can result in a significant difference of PDR diagnostic results ($10^{1.2}$ and $10^{-0.4}$ times different for n and G_0, respectively, when compared with the values from K99). It also indicates that, unless a further detailed analysis is made of model predications, it is wise not to take the above parameters too literally, because uncertainties of chemistry and microphysics in PDR models, including the dust grain models, PE heating rates, reaction coefficients of chemical

network, molecular/atomic parameters, radiation transfer problems and assumptions for metallicity, still play important roles in PDR diagnostics.

5 CONCLUSIONS

We present a numerical study of [O I], [C II] and [C I] emissions from PDR using CLOUDY. We produce PDR infrared diagnostic diagrams, which show how the intensities and line ratios of the studied PDR diagnostic lines vary as functions of the PDR density and the strength of incident FUV fields.

We make direct comparisons between the calculated PDR surface gas temperatures and the infrared diagnostic diagrams from our work and from K99. We find that significant differences exist in our parameter space. The different treatments of dust grain physics, the change of H_2 formation and dissociation rates and the improvement in the radiation transfer in our CLOUDY models are likely to be the major reasons for the divergences in the diagnostic emission predications.

Our PDR diagnostic diagrams are based on the up-to-date theory and coefficients for PDR microphysics and chemistry, which represent a current improved solution of PDR diagnostics and can be used to evaluate the physical properties of the observed PDRs. Meanwhile, the uncertainties of chemistry and microphysics in PDR models still play important roles in the accuracy of PDR diagnostics, and therefore caution should be exercised when interpreting observational data.

References

Abel, N. P., Brogan, C. L., Ferland, G. J., O'Dell, C. R., Shaw, G., & Troland, T. H. 2004, ApJ, 609, 247
Abel, N. P., Ferland, G. J., Shaw, G., & van Hoof, P. A. M. 2005, ApJS, 161, 65
Abgrall, H., Le Bourlot, J., Pineau Des Forets, G., Roueff, E., Flower, D. R., & Heck, L. 1992, A&A, 253, 525
Bakes, E. L. O., & Tielens, A. G. G. M. 1994, ApJ, 427, 822
Bertoldi, F., & Draine, B. T. 1996, ApJ, 458, 222
Burton, M. G., Hollenbach, D. J., & Tielens, A. G. G. M. 1990, ApJ, 365, 620
Cazaux, S., & Tielens, A. G. G. M. 2002, ApJ, 575, L29
Contursi, A., et al. 2002, AJ, 124, 751
de Jong, T., Boland, W., & Dalgarno, A. 1980, A&A, 91, 68
Draine, B. T., & Bertoldi, F. 1996, ApJ, 468, 269
Ferland, G. J., Korista, K. T., Verner, D. A., Ferguson, J. W., Kingdon, J. B., & Verner, E. M. 1998, PASP, 110, 761
Habing, H. J. 1968, Bull. Astron. Inst. Netherlands, 19, 421
Hollenbach, D. J., & Tielens, A. G. G. M. 1999, Reviews of Modern Physics, 71, 173
Hunter, D. A., et al. 2001, ApJ, 553, 121
Jura, M. 1974, ApJ, 191, 375
Kaufman, M. J., Wolfire, M. G., Hollenbach, D. J., & Luhman, M. L. 1999, ApJ, 527, 795
Le Teuff, Y. H., Millar, T. J., & Markwick, A. J. 2000, A&AS, 146, 157
Meijerink, R., Spaans, M., & Israel, F. P. 2007, A&A, 461, 793
Minamidani, T., et al. 2008, ApJS, 175, 485
Okada, Y., Onaka, T., Shibai, H., & Doi, Y. 2003, A&A, 412, 199
Pellegrini, E. W., et al. 2007, ApJ, 658, 1119
Röllig, M., Ossenkopf, V., Jeyakumar, S., Stutzki, J., & Sternberg, A. 2006, A&A, 451, 917
Röllig, M., et al. 2007, A&A, 467, 187
Savage, B. D., & Sembach, K. R. 1996, ARA&A, 34, 279
Stoerzer, H., Stutzki, J., & Sternberg, A. 1996, A&A, 310, 592
Stutzki, J., et al. 1997, ApJ, 477, L33
Tielens, A. G. G. M., & Hollenbach, D. 1985, ApJ, 291, 722
van Dishoeck, E. F., & Black, J. H. 1986, ApJS, 62, 109
van Hoof, P. A. M., et al. 2001, in ASP Conf. Ser. 247, Spectroscopic Challenges of Photoionized Plasmas, 363
van Hoof, P. A. M., Weingartner, J. C., Martin, P. G., Volk, K., & Ferland, G. J. 2004, MNRAS, 350, 1330
Wolfire, M. G., Tielens, A. G. G. M., & Hollenbach, D. 1990, ApJ, 358, 116